

# Investigation on structural, thermal, optical and sensing properties of meta-stable hexagonal MoO<sub>3</sub> nanocrystals of one dimensional structure

Angamuthuraj Chithambararaj and Arumugam Chandra Bose\*§

## Full Research Paper

Open Access

Address:  
Nanomaterials Laboratory, Department of Physics, National Institute of Technology, Tiruchirappalli – 620 015, India

Email:  
Angamuthuraj Chithambararaj - a.chithambararaj@gmail.com;  
Arumugam Chandra Bose\* - acbose@nitt.edu

\* Corresponding author  
§ Tel: +91-9444065746; Fax: 91-431-2500133

Keywords:  
fiber optic sensor; hexagonal phase; molybdenum oxide; one dimensional rod; phase transition

*Beilstein J. Nanotechnol.* **2011**, *2*, 585–592.  
doi:10.3762/bjnano.2.62

Received: 01 April 2011  
Accepted: 02 August 2011  
Published: 14 September 2011

Associate Editor: J. J. Schneider

© 2011 Chithambararaj and Bose; licensee Beilstein-Institut.  
License and terms: see end of document.

## Abstract

Hexagonal molybdenum oxide (h-MoO<sub>3</sub>) was synthesized by a solution based chemical precipitation technique. Analysis by X-ray diffraction (XRD) confirmed that the as-synthesized powder had a metastable hexagonal structure. The characteristic vibrational band of Mo–O was identified from Fourier transform infrared spectroscopy (FT-IR). Scanning electron microscopy (SEM) and transmission electron microscopy (TEM) images clearly depicted the morphology and size of h-MoO<sub>3</sub>. The morphology study showed that the product comprises one-dimensional (1D) hexagonal rods. From the electron energy loss spectroscopy (EELS) measurement, the elemental composition was investigated and confirmed from the characteristic peaks of molybdenum and oxygen. Thermogravimetric (TG) analysis on metastable MoO<sub>3</sub> revealed that the hexagonal phase was stable up to 430 °C and above this temperature complete transformation into a highly stable orthorhombic phase was achieved. The optical band gap energy was estimated from the Kubelka–Munk (K–M) function and was found to be 2.99 eV. Finally, the ethanol vapor-sensing behavior was investigated and the sensing response was found to vary linearly as a function of ethanol concentration in the parts per million (ppm) range.

## Introduction

Considerable research interest has been focused on metastable nanocrystalline materials due to their unusual and enhanced properties as compared to their bulk counterparts. Synthesis of metastable nanocrystals with controlled size and shape has

always been one of the most fascinating challenges as the properties of nanomaterials are essentially determined by their phase, shape, size and chemical composition [1]. Recently, molybdenum oxide and its compounds have aroused interest for

various potential applications, such as gas sensors, highly reactive catalysts, high optical contrast electrochromic devices and cathodic electrodes for lithium batteries, due to their unique structural, optical and electrical properties [2-5]. Several synthetic techniques have been developed for controlled synthesis of nanocrystalline MoO<sub>3</sub> materials [6-11]. Recently, Dhage et al. [12], Ramana et al. [13] and Song et al. [14] have prepared h-MoO<sub>3</sub> and studied its structural and thermal properties. Zheng et al. prepared highly dispersed h-MoO<sub>3</sub> through a solution-based technique and investigated its photochromic and electrochromic properties [4]. By adjusting the hydrothermal reaction temperature, metastable (h-MoO<sub>3</sub>) and stable ( $\alpha$ -MoO<sub>3</sub>) MoO<sub>3</sub> nanoparticles were successfully synthesized by Chithambararaj et al. [15].

Thus, many research articles are focused on the synthesis of h-MoO<sub>3</sub> as opposed to the stable  $\alpha$ -MoO<sub>3</sub>, due to the reduced crystallite size and one dimensional growth. Usually, the  $\alpha$ -MoO<sub>3</sub> is a stable structure formed at a higher temperature relative to the metastable h-MoO<sub>3</sub>. Thus, there is a phase transformation from h-MoO<sub>3</sub> to  $\alpha$ -MoO<sub>3</sub> at 400 °C, which is inferred from TGA/DTA studies [14,16]. With an increase in temperature, the crystallites aggregate and promote rapid growth of the particle. Hence, crystallite size in the nanometer range is difficult to control in the case of  $\alpha$ -MoO<sub>3</sub>.

The present work demonstrates the synthesis of metastable h-MoO<sub>3</sub> material through a solution-based chemical precipitation technique. The structure, shape and size of the as-synthesized sample were characterized by XRD, SEM and TEM analysis. The effects of the crystallite size and strain, on the diffraction peak broadening, were deconvoluted and their values were estimated using Scherrer and Wagner–Aqua methods. The phase stability and its transformation into a highly stable orthorhombic structure were confirmed by thermal studies. The optical band structure and ethanol vapor-sensing behavior were studied by means of diffuse reflectance spectroscopy (DRS) and fiber optics spectroscopy, respectively. To the best of our knowledge, this paper reports for the first time the ethanol vapor-sensing mechanism with h-MoO<sub>3</sub> by fiber optics sensor.

## Results and Discussion

### Crystal phase analysis

The XRD pattern of the as-synthesized MoO<sub>3</sub> powder is shown in Figure 1. The sample product crystallizes in the hexagonal phase of MoO<sub>3</sub>, and the diffraction peaks are indexed with reference to a standard (JCPDS-21-0569:  $a = 10.522$  Å and  $c = 14.888$  Å) data file. No secondary impurity peaks corresponding to other polymorphs of MoO<sub>3</sub>, namely orthorhombic or monoclinic, are present. From the XRD pattern, the high intensity peak observed at 26.5° is broadened in comparison to the

bulk compound. The observed broadening is a convolution of the instrumental error, the reduced crystallite size and the existence of microstrain in the synthesized sample product.

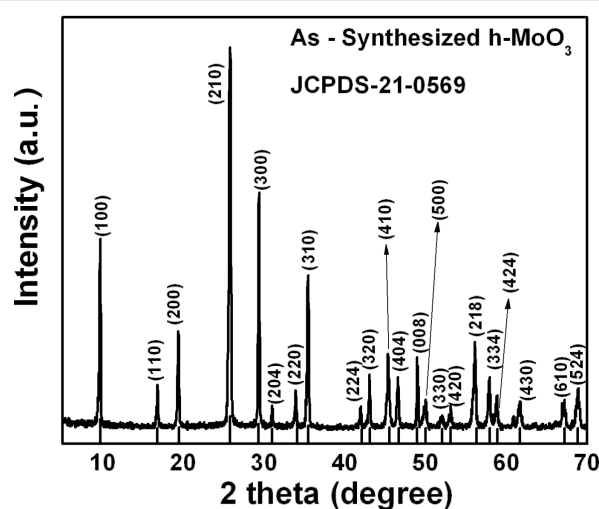


Figure 1: XRD pattern of as-synthesized h-MoO<sub>3</sub>.

The overall contribution to the broadening is expressed as  $\beta_{hkl} = \beta_{ins} + \beta_{size} + \beta_{strain}$ , where  $\beta_{ins}$  is the full width at half maximum (FWHM) due to instrumental error, and  $\beta_{size}$  and  $\beta_{strain}$  are the FWHM due to the crystallite size and strain, respectively. The broadening due to instrumental error is eliminated by the Rachinger method [17]

$$\beta_{hkl} = \beta_{obs} - \frac{\beta_{ins}^2}{\beta_{obs}}, \quad (1)$$

where  $\beta_{obs}$  and  $\beta_{hkl}$  refer to the FWHM of observed and measured sample profiles, respectively. In order to study the crystallite size and strain effect on the peak broadening, Scherrer [18] and Wagner–Aqua (W–A) [17] methods were considered. The Scherrer method is used to calculate the crystallite size ( $D_{hkl}$ ) with the assumption of negligible strain,

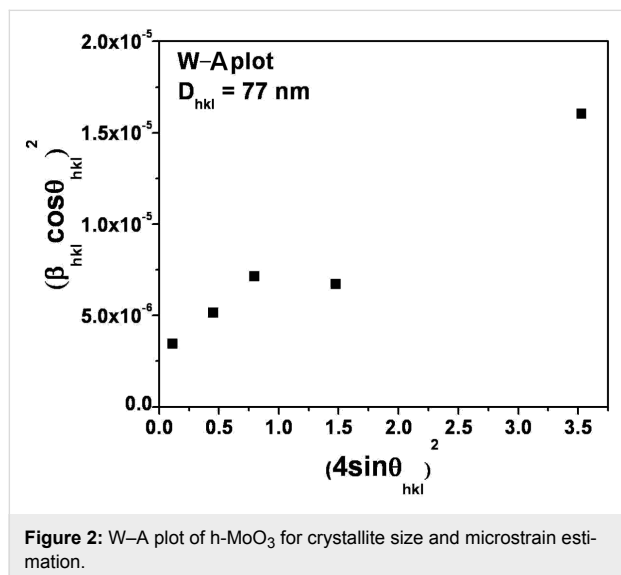
$$D_{hkl} = \frac{K\lambda}{\beta_{size} \cos \theta_{hkl}}, \quad (2)$$

where  $K$  is the shape factor (0.9),  $\lambda$  is the wavelength of Cu K $\alpha_1$  radiation (1.5406 Å), and  $\theta_{hkl}$  is the Bragg diffraction angle. The crystallite size was estimated and found to be 51 nm. Although the size of the crystallite is in the nanometer range, significant structural defects such as dislocations, stacking faults, twin boundaries and intergrowth, etc., induce strain in the material, which results in considerable broadening of the diffract-

tion peak profile. In order to distinguish and deconvolute the crystallite size and strain effects on the peak broadening, the W–A method is adopted and the equation is

$$(\beta_{hkl} \cos \theta_{hkl})^2 = \left( \frac{K\lambda}{D_{hkl}} \right)^2 + (4\epsilon_{hkl} \sin \theta_{hkl})^2. \quad (3)$$

Figure 2 shows the W–A plot for the as-synthesized sample. To determine the crystallite size and strain, a graph was plotted with  $(4\sin\theta_{hkl})^2$  along the X-axis and  $(\beta_{hkl}\cos\theta_{hkl})^2$  along the Y-axis. From the linear fit, the crystallite size ( $D_{hkl}$ ) was extracted from the Y-intercept and the microstrain ( $\epsilon_{hkl}$ ) from the slope of the fit.



The crystallite size and strain were estimated from the graph and the values are 77 nm and  $3.509 \times 10^{-6}$ , respectively. From these results, it is clearly confirmed that the observed broadening in the XRD peaks is mainly due to the smaller crystallite size.

### Functional group analysis

The functional groups present in  $\text{MoO}_3$  are identified through FT-IR analysis and are shown in Figure 3. A small band at  $3434 \text{ cm}^{-1}$  and a sharp band at  $1616 \text{ cm}^{-1}$  correspond to the stretching and bending vibrations, respectively, of the hydrogen bonded –OH group in water molecules.

Distinct peaks at  $3219 \text{ cm}^{-1}$  and at  $1404 \text{ cm}^{-1}$  are attributed to the stretching and bending vibrations of N–H in  $\text{NH}_4^+$ . These results are consistent with the previously reported results [19]. The peaks between  $1000 \text{ cm}^{-1}$  and  $900 \text{ cm}^{-1}$  are ascribed to the Mo=O characteristic stretching vibration of the hexagonal

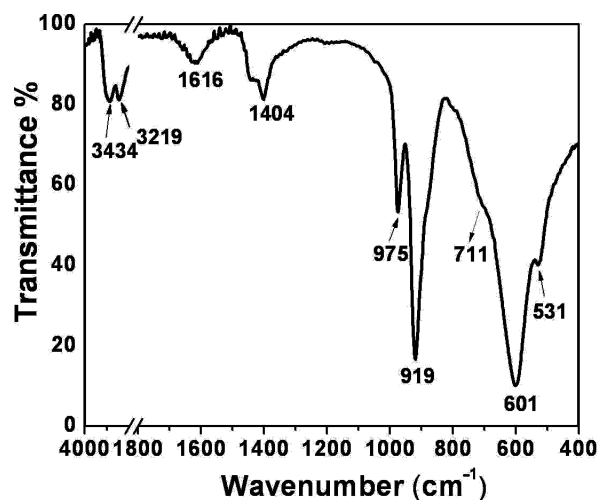


Figure 3: FT-IR spectrum of as-synthesized h-MoO<sub>3</sub>.

phase. A broad and complex band peaked at  $600 \text{ cm}^{-1}$  corresponds to the Mo–O vibration [14].

### Surface morphology and particle size analysis

Figure 4 displays the low and high magnification SEM images of as-synthesized h-MoO<sub>3</sub> powder. From Figure 4a, the particles are widely distributed and are found to be aggregated in a spherical structure whose diameter is in the micron range and comprises a bunch of nanorods. The corresponding high magnification images (Figure 4b–d) show that the particles are in the form of one-dimensional hexagonal rods. A typical TEM image of the as-synthesized particle is shown in Figure 5. It clearly illustrates that the as-synthesized powder comprises 1D structures of ~200 nm diameter and length of about 800 nm.

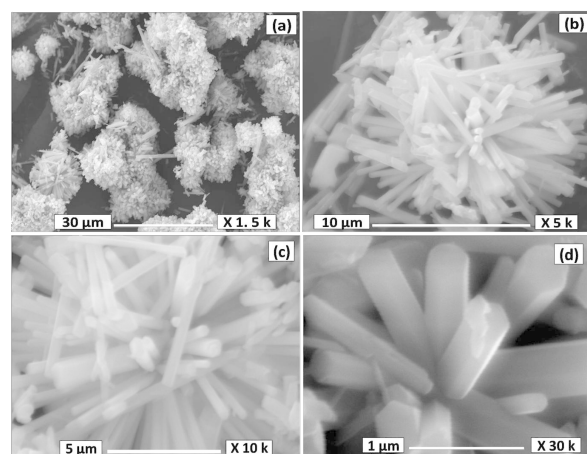
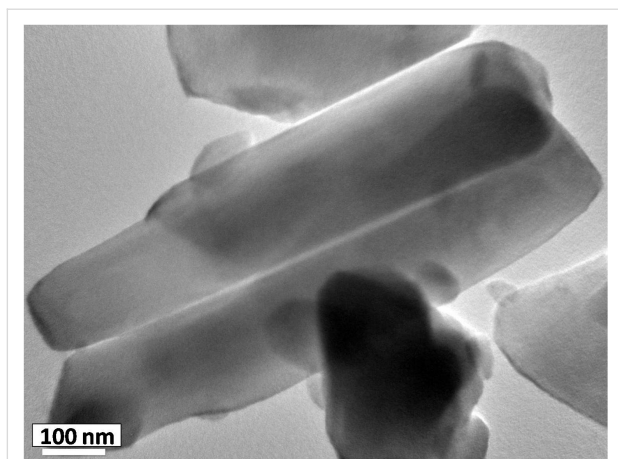
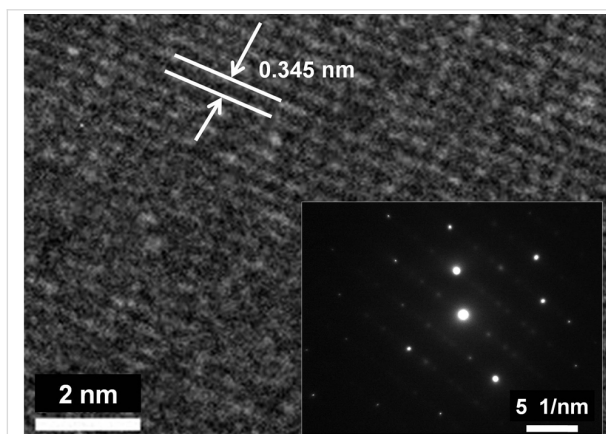


Figure 4: Low and high magnification SEM micrographs of h-MoO<sub>3</sub>.



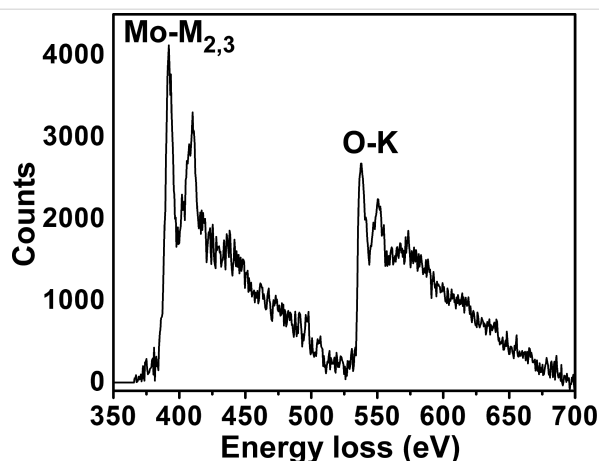
**Figure 5:** TEM micrograph of the one-dimensional structure of h-MoO<sub>3</sub>.

Figure 6 shows the HRTEM image and the inset is the corresponding SEAD pattern of h-MoO<sub>3</sub>. From the lattice resolved HRTEM image, the distance between the two planes was found to be 0.345 nm, belonging to the (210) plane of h-MoO<sub>3</sub>. The electron diffraction, with a highly intense dotted pattern, reveals the single crystalline nature of h-MoO<sub>3</sub>. Furthermore, the elemental composition and chemical bonding information were confirmed by EELS investigation.



**Figure 6:** HRTEM image of an as-synthesized h-MoO<sub>3</sub> nanorod and their electron diffraction pattern (inset).

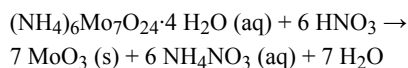
Figure 7 depicts the typical EELS profile of an individual hexagonal rod. It shows two distinct edges at 532 eV (oxygen K edge) and 382 eV (molybdenum M edge), confirming the presence of only O and Mo with a covalent interaction [20]. The observed O-K edge peak reflects the electronic transitions from the oxygen 1 s core level to the unoccupied final state of O 2p hybridized with the Mo 4d state [21], and the Mo-M<sub>2,3</sub> peak is due to excitation from 3p<sub>1/2</sub> and 3p<sub>3/2</sub> core level electrons to unoccupied states (4d and 5s) of molybdenum [22].



**Figure 7:** EELS spectrum of resultant h-MoO<sub>3</sub>.

### Growth mechanism and formation of 1D h-MoO<sub>3</sub>

On the basis of experimental results, the possible mechanism for the formation of h-MoO<sub>3</sub> is outlined as follows: In the present work, (NH<sub>4</sub>)<sub>6</sub>Mo<sub>7</sub>O<sub>24</sub>·4 H<sub>2</sub>O and HNO<sub>3</sub> are used as reactant precursors for the synthesis of h-MoO<sub>3</sub> nanocrystals. As per the following reaction Equation, MoO<sub>6</sub> is considered as an initial seed nucleus for the formation of MoO<sub>3</sub>.



Here, molybdenum is located at the center and six oxygen atoms are coordinated in octahedral sites. During the nucleation, these octahedral structures interact with each other through corners (a-axis) and edges (c-axis) by means of electrostatic interactions between NH<sub>4</sub><sup>+</sup> and OH<sup>−</sup> ions. The stacking and assembling of these octahedral structures result in the formation of a stable hexagonal structure. Thus, the NH<sub>4</sub><sup>+</sup> functional group present in the reaction condition acts indirectly as a structure directing agent [4,23]. Moreover, the initial seed nuclei formed during the nucleation stage are composed of hexagonal unit cells which can induce anisotropic growth along the c-axis, and thus hexagonal shaped nanocrystals with 1D structure are favored [24,25].

### Thermal analysis

The thermal behavior was studied in detail and is depicted in Figure 8. From the TG and DTG graph, the first weight loss (2.33 wt %) in the 70–190 °C region corresponds to vaporization of the hydrogen bonded water molecules that are physically adsorbed on the surface of the MoO<sub>3</sub>. The second weight loss (1.13 wt %) takes place between 190 and 270 °C, due to vaporization of gaseous nitrates and ammonia compounds from the material.

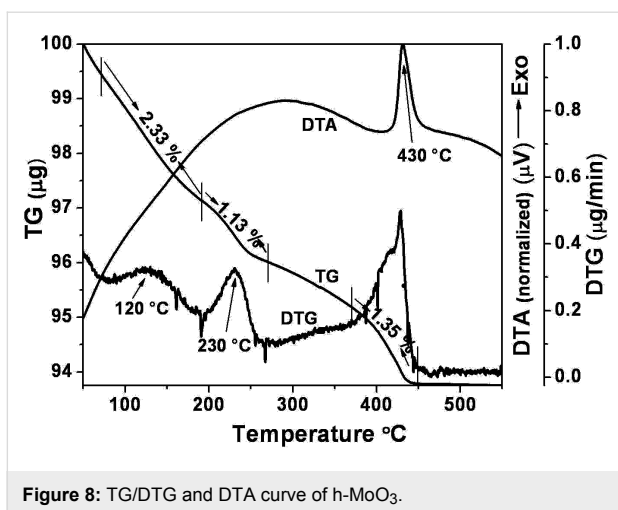


Figure 8: TG/DTG and DTA curve of h-MoO<sub>3</sub>.

The same observation is made from the DTA curve, which exhibits two broad exothermic peaks well below 270 °C. After dehydration and removal of ammonia compounds, a sharp exothermic peak at 430 °C with weight loss of 1.35 wt % is attributed to liberation of coordinated water and ammonia molecules from the internal structure of the MoO<sub>3</sub> material, which promotes an irreversible phase transformation from the hexagonal to the orthorhombic structure [14,16]. The powder subjected to TGA measurements was subjected to XRD analysis, and the result confirmed that above 450 °C the product is in a stable orthorhombic structure (Figure not included). Above 450 °C no changes in the TG/DTA curve are seen revealing that the thermodynamically stable  $\alpha$ -MoO<sub>3</sub> was achieved.

### Optical absorption studies

The optical absorption behavior and band gap energy of h-MoO<sub>3</sub> was studied by means of DRS, as shown in Figure 9. The spectrum shows a maximum reflectance in the region between 600 nm and 450 nm corresponding to lower absorption. At 420 nm, a decrease in reflectance is seen due to fundamental absorption (valance band to conduction band) by the material [26]. Further, the optical band gap is evaluated using K–M function as follows [27]:

$$F(R_{\infty}) = \frac{(1 - R_{\infty})^2}{2R_{\infty}} = \frac{K(\lambda)}{s(\lambda)} \propto \alpha = \frac{(h\nu - E_g)^2}{h\nu}, \quad (4)$$

where  $F(R_{\infty})$  is the K–M function or re-emission function,  $R_{\infty}$  is the diffuse reflectance of an infinitely thick sample,  $K(\lambda)$  is the absorption coefficient,  $s(\lambda)$  is the scattering coefficient,  $h\nu$  is the photon energy and  $E_g$  is the band gap energy for indirect transition.

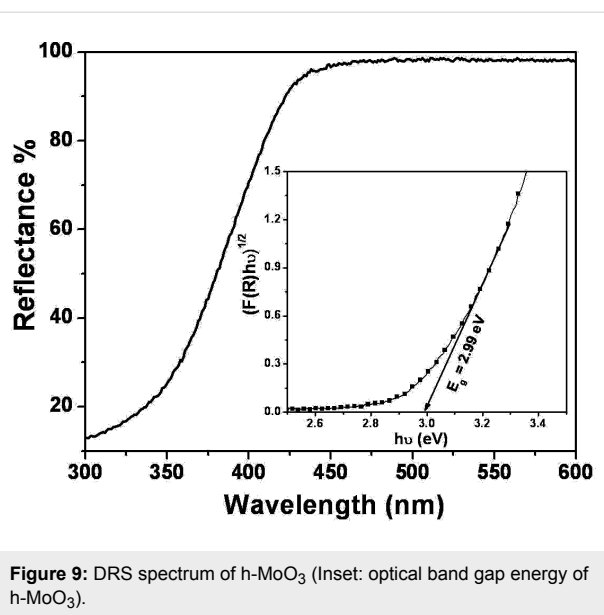


Figure 9: DRS spectrum of h-MoO<sub>3</sub> (Inset: optical band gap energy of h-MoO<sub>3</sub>).

The indirect optical band gap energy is determined by extrapolating the linear portion of the plots of  $(F(R_{\infty})h\nu)^{1/2}$  versus  $(h\nu)$  shown as an inset in Figure 9. The estimated energy band gap value is about 2.99 eV and is considerably higher than that of the bulk (2.95 eV). This increase in  $E_g$  is attributed to the reduced particle size.

### Sensor study

The ethanol vapor-sensing behavior was examined by means of an optical fiber sensor setup and analyzed on the basis of simultaneous changes in the refractive index and evanescent wave absorption. In our experiment, a portion of the fiber cladding (~3 cm) was partially removed and coated with as-synthesized h-MoO<sub>3</sub>; this is considered as the sensing area. In the sensor study, the characteristic spectrum as a function of wavelength in the range of 200–1100 nm was recorded for different ethanol concentrations. The recorded spectrum is shown in Figure 10 and the inset represents the magnified view of the spectra recorded in the range between 600 and 800 nm. In this plot, the Y-axis denotes the intensity, measured in counts, for each concentration of ethanol. The ethanol concentration was increased from 0 to 500 ppm in increments of 50 ppm. From Figure 10, it is clearly seen that the intensity peaks are a maximum at 684, 764 and 935 nm. The magnified spectrum, shown as an inset, clearly shows the gradual increase and variation in intensity with increase in ethanol concentration. The gas sensitivity is calculated using the formula

$$\text{sensitivity} = \text{counts} / \text{ppm (Ethanol)} \quad (5)$$

The sensitivity is estimated by plotting a separate graph of ethanol concentration (in ppm) versus intensity (in counts) for

each value of  $\lambda_{\max}$  (684, 764 and 935 nm respectively). The plot is depicted in Figure 11: The slope of the curve determines the sensitivity and is found to be 74, 67 and 26 counts/ppm for  $\lambda_{\max} = 684, 764$  and 935 nm, respectively. From the plot, the maximum sensitivity is seen for  $\lambda_{\max} = 684$  nm.

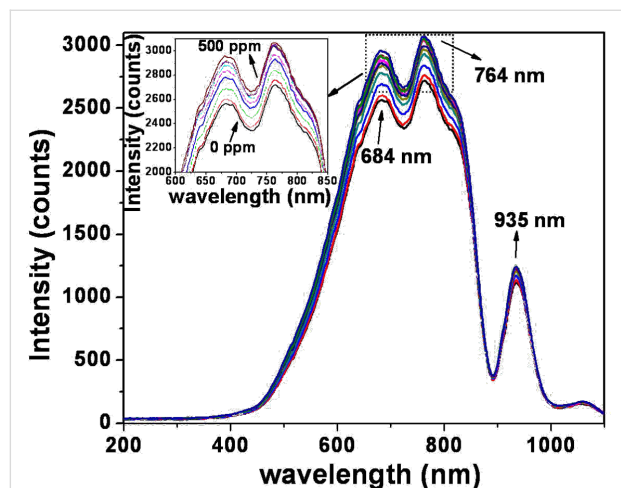


**Figure 10:** Spectral response of h-MoO<sub>3</sub> for varying concentration of ethanol in ppm.

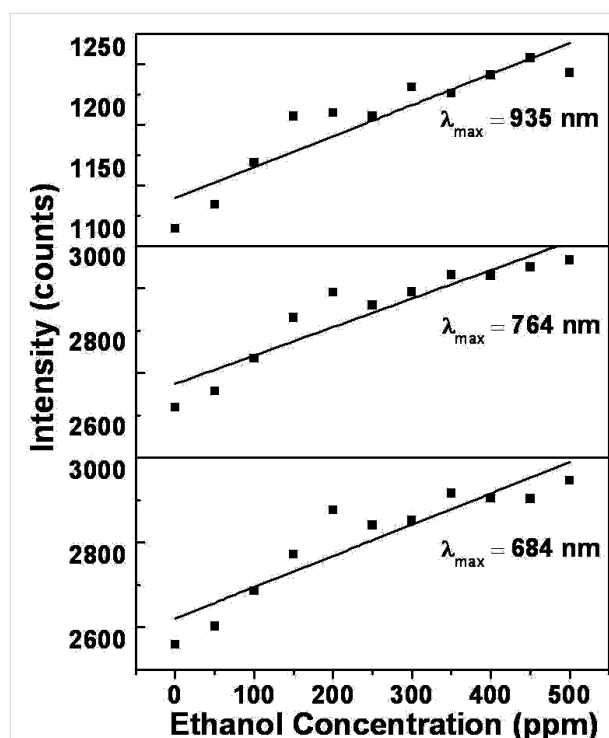


**Figure 11:** Plot of peak intensity versus ethanol concentration for values  $\lambda_{\max} = 684, 764$  and 935 nm.

Here, it is proposed that the gas sensing mechanism follows the changes in the refractive index and evanescent wave absorption.

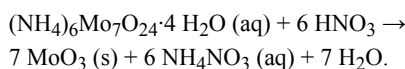
For h-MoO<sub>3</sub>, the oxygen vacancies and interstitial molybdenum atoms play a major role in gas sensing operation. The reaction between ethanol gas and the chemisorbed oxygen ( $O_2^-$ ,  $O^-$  and  $O^{2-}$ ) at the surface of the MoO<sub>3</sub> material changes the refractive index of the clad structure. Due to this change, the light wave travelling through the removed and coated portion of the cladding experiences a change in the evanescent wave absorption [28–32]. Thus, the resultant intensity recorded in the spectrum is a sum of changes due to refractive index and evanescent wave absorptions.

## Conclusions

In summary, metastable h-MoO<sub>3</sub> was prepared by a solution-based chemical precipitation technique. The metastable hexagonal phase was confirmed by XRD. The crystallite size of the h-MoO<sub>3</sub> was in nanometer range and the corresponding strain was in the order of  $10^{-6}$ . The metal–oxygen vibrational states (M=O and M–O) were identified from the vibrational spectrum. The one-dimensional hexagonal rod structure, with regular arrangement and preferred orientation, was observed in SEM, TEM and HRTEM images. From EELS, the O-K edge and Mo-M<sub>2,3</sub> peaks confirmed the existence of molybdenum and oxygen. From thermal analysis, the structural transformation from hexagonal to stable orthorhombic was observed at 430 °C. A formation and growth mechanism for the h-MoO<sub>3</sub> nanocrystals with 1D structure was proposed. The estimated band gap was 2.99 eV from the optical absorption studies. Finally, the ethanol vapor-sensing behavior was investigated and the sensor response increased linearly as a function of ethanol concentration in the range of 0 to 500 ppm. In the present study, changes in the refractive index and the evanescent wave absorption phenomenon were proposed to explain the gas sensing mechanism. The reaction between ethanol gas and the chemisorbed oxygen ( $O_2^-$ ,  $O^-$  and  $O^{2-}$ ) at the surface of the MoO<sub>3</sub> material simultaneously changes the refractive index and evanescent wave absorption thereby varying the intensity at the detector.

## Experimental

All the chemicals were purchased from Merck and were used without any further purification. Ammonium heptamolybdate tetrahydrate (AHM) was dissolved in distilled water (10 mL), to give a concentration of 0.2 M. A homogeneous solution was obtained after stirring for 15 minutes and was then mixed with concentric nitric acid (5 mL). The mixture was then heated at 85 °C for 1 h and the resulting precipitate was subsequently washed and centrifuged with distilled water several times. The obtained powder was dried at 70 °C in vacuum for 6 h. Thus, by a chemical precipitation technique, the h-MoO<sub>3</sub> nanocrystal was synthesized by acid decomposition of ammonium molybdate according to the following reaction equation,



The crystalline phase was analyzed by XRD using a Ultima III Rigaku X-ray diffractometer with Cu K $\alpha_1$  radiation (1.5406 Å), in the range of 5–80° in steps of 0.2 °/min. We eliminated the peak broadening due to instrumental error by performing control experiments with a standard silicon sample and hence accounting for the error properly in the estimation of the crystallite size and strain. FT-IR was recorded on a PerkinElmer spectrometer. For FT-IR measurements, the pellet was prepared by mixing synthesized powder with KBr, and the spectra were recorded in the range of 4000–400 cm<sup>−1</sup>. To examine the surface morphology and particle shape, the powder was uniformly sprayed on carbon tape; a gold coating was made on the sample for 30 s and the micrographs were obtained at various magnifications by means of SEM (Model S3000-Hitachi). TEM, high resolution TEM (HRTEM) images and EELS spectrum were acquired by means of a JEOL model JEM FX II 2000 instrument. The thermal behavior was analyzed by means of an EXSTAR6200 thermal analyzer at a heating rate of 10 °C/min, from room temperature to 550 °C in air. The weight loss and the corresponding phase transition were observed by thermal gravimetric (TG), differential thermal gravimetric (DTG) and differential thermal analysis (DTA). The optical properties of h-MoO<sub>3</sub> were studied by DRS and were recorded by means of a computer controlled T90+ UV–vis spectrophotometer. A BaSO<sub>4</sub> plate was used as a reference (100% reflectance), on which a fine-ground powder was pressed. The spectrum was recorded at room temperature in the wavelength range 230–700 nm at a rate of 1 nm/s. Ethanol vapor sensing was performed with a fiber optics sensor arrangement with a white light source (Model SL1, StellarNet Inc., USA with wavelength range from 200 to 2000 nm) and a miniature fiber optics spectrometer (EPP-2000, StellarNet Inc, USA) having a spectral range of 100 to 1100 nm. Poly methyl methacrylate (PMMA) based multimode plastic step index fiber (length 100 cm, diameter 700 μm and numerical aperture 0.51) with cleaved ends was used. The clad region of the fiber was partially removed (about a length of 3 cm) and the surface was polished. The polished surface was coated with h-MoO<sub>3</sub>. A round bottom flask (1000 mL) was used as the gas chamber into which the fiber optic sensor was inserted. An ethanol solution of concentration 0–500 ppm was prepared and used in the gas chamber for sensor measurement.

## Acknowledgements

This research was financially supported by NRB-DRDO project (DNRD/05/4003/NRB/143), Government of India. We thank Prof. D. Sastikumar and Dr. R. Justin Joseyphus for sensor and thermal studies.

## References

1. Tjong, S. C. *Nanocrystalline Materials; Their Synthesis-Structure-Property Relations and Applications*; Elsevier: Amsterdam, Boston, 2006.
2. Mariotti, D.; Lindstrom, H.; Bose, A. C.; Ostrikov, K. *Nanotechnology* **2008**, *19*, 495302. doi:10.1088/0957-4484/19/49/495302
3. Subba Reddy, C. V.; Qi, Y. Y.; Jin, W.; Zhu, Q. Y.; Deng, Z. R.; Chen, W.; Mho, S. J. *Solid State Electrochem.* **2007**, *11*, 1239–1243. doi:10.1007/s10008-007-0278-4
4. Zheng, L.; Xu, Y.; Jin, D.; Xie, Y. *Chem. Mater.* **2009**, *21*, 5681–5690. doi:10.1021/cm9023887
5. Taurino, A. M.; Forleo, A.; Francioso, L.; Siciliano, P. *Appl. Phys. Lett.* **2006**, *88*, 152111. doi:10.1063/1.2192571
6. Navas, I.; Vinodkumar, R.; Lethy, K. J.; Dettý, A. P.; Ganesan, V.; Sathe, V.; Pillai, V. P. M. *J. Phys. D: Appl. Phys.* **2009**, *42*, 175305. doi:10.1088/0022-3727/42/17/175305
7. Zhao, Y.; Liu, J.; Zhou, Y.; Zhang, Z.; Xu, Y.; Naramoto, H.; Yamamoto, S. *J. Phys.: Condens. Matter* **2003**, *15*, L547–L552. doi:10.1088/0953-8984/15/35/101
8. Siciliano, T.; Tepore, A.; Filippo, E.; Micocci, G.; Tepore, M. *Mater. Chem. Phys.* **2009**, *114*, 687–691. doi:10.1016/j.matchemphys.2008.10.018
9. Yan, B.; Zheng, Z.; Zhang, J.; Gong, H.; Shen, Z.; Huamg, W.; Yu, T. *J. Phys. Chem. C* **2009**, *113*, 20259–20263. doi:10.1021/jp907602w
10. Subba Reddy, C. V. S.; Walker, E. H., Jr.; Wen, C.; Mho, S. *J. Power Sources* **2008**, *183*, 330–333. doi:10.1016/j.jpowsour.2008.05.005
11. Badica, P. *J. Cryst. Growth* **2007**, *7*, 794–801. doi:10.1021/cg060893s
12. Dhage, S. R.; Hassan, M. S.; Yang, O.-B. *Mater. Chem. Phys.* **2009**, *114*, 511–514. doi:10.1016/j.matchemphys.2008.10.076
13. Ramana, C. V.; Atuchin, V. V.; Troitskaia, I. B.; Gromilov, S. A.; Kostrovsky, V. G.; Saupe, G. B. *Solid State Commun.* **2009**, *149*, 6–9. doi:10.1016/j.ssc.2008.10.036
14. Song, J.; Ni, X.; Geo, L.; Zheng, H. *Mater. Chem. Phys.* **2007**, *102*, 245–248. doi:10.1016/j.matchemphys.2006.12.011
15. Chithambararaj, A.; Bose, A. C. *J. Alloys Compd.* **2011**, *509*, 8105–8110. doi:10.1016/j.jallcom.2011.05.067
16. Michailovski, A.; Krumeich, F.; Patzke, G. R. *Chem. Mater.* **2004**, *16*, 1433–1440. doi:10.1021/cm0311731
17. Pratap, R. *J. Mater. Sci.* **1974**, *10*, 1011–1015.
18. Yogamalar, R.; Srinivasan, R.; Vinu, A.; Ariga, K.; Bose, A. C. *Solid State Commun.* **2009**, *149*, 1919–1923. doi:10.1016/j.ssc.2009.07.043
19. Muraoka, Y.; Grenier, J. C.; Petit, S.; Pouchard, M. *Solid State Sci.* **1999**, *1*, 133–148. doi:10.1016/S1293-2558(00)80070-9
20. Hu, S.; Wang, X. *J. Am. Chem. Soc.* **2008**, *130*, 8126–8127. doi:10.1021/ja801448c
21. Wu, G.; Sekiguchi, T.; Baba, Y.; Shimoyama, I. *Nucl. Instrum. Methods Phys. Res., Sect. B* **2006**, *245*, 406–410. doi:10.1016/j.nimb.2005.11.004
22. Diaz, C.; Lavayen, V.; O'Dwyer, C. J. *Solid State Chem.* **2010**, *183*, 1595–1603. doi:10.1016/j.ssc.2010.05.006
23. Lunk, H. J.; Hartl, H.; Monika, A.; Fait, M. J. G.; Shenderovic, I. G.; Feist, M.; Frisk, T. A.; Daemen, L. L.; Mauder, D.; Eckelt, R.; Gurinov, A. A. *Inorg. Chem.* **2010**, *49*, 9400–9408. doi:10.1021/ic101103g
24. Xia, Y.; Yang, P.; Sun, Y.; Wu, Y.; Mayers, B.; Gates, B.; Yin, Y.; Kim, F.; Yan, H. *Adv. Mater.* **2003**, *15*, 353–389. doi:10.1002/adma.200390087

25. Wei, Y.; Lu, F.; Zhang, X.; Chen, D. *Chem. Mater.* **2006**, *18*, 5733–5737. doi:10.1021/cm0606171
26. He, T.; Yao, J. *J. Photochem. Photobiol., C* **2003**, *4*, 125–143. doi:10.1016/S1389-5567(03)00025-X
27. Liu, J.; Lu, Y.; Liu, J.; Yang, X.; Yu, X. *J. Alloys Compd.* **2010**, *496*, 261–264. doi:10.1016/j.jallcom.2010.01.053
28. Yogamalar, R.; Mahendran, V.; Srinivasan, R.; Beitollahi, A.; Pradeep Kumar, R.; Bose, A. C.; Vinu, A. *Chem.–Asian J.* **2010**, *5*, 2379–2385. doi:10.1002/asia.201000358
29. Renganathan, B.; Sastikumar, D.; Gobi, G.; Yogamalar, N. R.; Bose, A. C. *Sens. Actuators, B* **2011**, *152*, 263–270. doi:10.1016/j.snb.2011.04.031
30. Ge, C.; Xie, C.; Cai, S. *Mater. Sci. Eng., B* **2007**, *137*, 53–58. doi:10.1016/j.mseb.2006.10.006
31. Comini, E.; Yubao, L.; Brando, Y.; Sberveglieri, G. *Chem. Phys. Lett.* **2005**, *407*, 368–371. doi:10.1016/j.cplett.2005.03.116
32. Barazzouk, S.; Tandon, R. P.; Hotchandani, S. *Sens. Actuators, B* **2006**, *119*, 691–694. doi:10.1016/j.snb.2006.01.026

## License and Terms

This is an Open Access article under the terms of the Creative Commons Attribution License (<http://creativecommons.org/licenses/by/2.0>), which permits unrestricted use, distribution, and reproduction in any medium, provided the original work is properly cited.

The license is subject to the *Beilstein Journal of Nanotechnology* terms and conditions: (<http://www.beilstein-journals.org/bjnano>)

The definitive version of this article is the electronic one which can be found at:  
[doi:10.3762/bjnano.2.62](https://doi.org/10.3762/bjnano.2.62)